In Situ Polymerization-Enabled Facile Electrode Interface in Solid-State Lithium-Metal Battery

Asish Kumar Das* and Sunil Kumar**

Department of Metallurgical Engineering and Materials Science, Indian Institute of Technology Indore, Simrol, 453552, India

Corresponding authors E-mail: *phd2201105011@iiti.ac.in, ** sunil@iiti.ac.in

Abstract:

Here, a ceramic-polymer composite membrane consisting of P(VDF-HFP), LiTFSI, and a high-entropy rhombohedral NASICON-structured ceramics filler $Li_{1.3}Al_{0.1}Sc_{0.1}Y_{0.1}Sn_{1.7/3}Zr_{1.7/3}Ti_{1.7/3}(PO_4)_3$ was employed as the solid electrolyte in the batteries. Further, the facile electrode interface was engineered via ring polymerization of 1,3-dioxolane (DOL) containing different lithium salts (LiTFSI, LiFSI, and LiDFOB) catalyzed by $LiPF_6$ salt. The synergistic effect of different salts provided a robust interphase at the lithium metal interface, enabling stable lithium plating/stripping in Li|Li coin cell configurations with a critical current density ~ 1 mA cm^{-2} at room temperature. The in situ polymerized matrix also facilitated the formation of potential lithium-ion conduit channels at the cathode side and the electrolyte-electrode interface, thereby mitigating key transport limitations that hinder the performance of conventional polymer electrolyte-based solid-state batteries. The Li|$LiFePO_4$ coin cell configuration demonstrated excellent cyclability with a discharge capacity of 107 mAh g^{-1} after 500 cycles at 1C.

Keywords: solid electrolytes; in situ polymerization, critical current density, ceramic-polymer composite, lithium metal batteries.

1. Introduction

As the demand for portable electronics, electric vehicles, and smart grids grows rapidly, lithium-ion batteries (LIBs) become indispensable to modern technology [1-5]. However, LIBs face intrinsic limitations such as specific capacity of graphite anodes (372 mAh g^{-1}), which constrains energy density compared to lithium metal (3860 mAh g^{-1}); the flammability and safety risks posed by organic liquid electrolytes; the narrow electrochemical stability window of conventional electrolytes, which limits the use of high-voltage cathodes; and performance degradation during fast charging due to lithium plating and dendrite formation [6]. Furthermore, to meet future energy storage requirements, solid-state lithium metal batteries (SLMBs) emerge as highly promising next-generation alternatives [7-9]. By combining a Li^+-conducting solid electrolyte with a high-capacity lithium metal anode, SLMBs not only eliminate flammable liquid electrolytes but also offer significantly higher energy density. Despite these advantages, their practical deployment is hindered by poor interfacial stability and high manufacturing costs, particularly due to challenges associated with scalable roll-to-roll fabrication. Therefore, the development of solid electrolytes that are simultaneously safe, stable, and compatible with metallic lithium is crucial for enabling the commercialization of SLMBs.

Solid polymer electrolytes (SPEs) are attractive candidates for SLMBs owing to their low cost, excellent processability, flexibility, and favorable interfacial contact with electrodes. Among them, polymer electrolytes based on poly(vinylidene fluoride-co-

hexafluoropropylene) [P(VDF-HFP)] have attracted significant attention due to their high dielectric constant, electrochemical stability at high oxidation voltages, and excellent mechanical flexibility [10, 11]. Despite these advantages, P(VDF-HFP)-based polymer electrolytes face inherent challenges that hinder their practical deployment in Li metal batteries. Their relatively low room-temperature lithium-ion conductivity limits rate capability, while insufficient mechanical strength reduces their ability to suppress lithium dendrite growth. Furthermore, residual solvents such as N, N-dimethylformamide can react with lithium metal, leading to interfacial instability. Nevertheless, polymer electrolytes exhibit low ionic conductivity at room temperature due to their semi-crystalline nature. Furthermore, conventional ex-situ solvent-assisted preparation routes often result in significant interfacial impedance, leading to degraded electrochemical performance of polymer electrolytes.

To circumvent these issues, composite polymer electrolytes incorporating ceramic fillers have emerged as an effective strategy [12]. Ceramic fillers can enhance conductivity by disrupting the crystalline domains of the polymer matrix, thereby increasing segmental chain motion and introducing faster lithium-ion transport pathways at the ceramic-polymer interface [13]. High-lithium-ion-conducting high-entropy ceramics, featuring multiple cations distributed over equivalent crystallographic sites, offer unique advantages [14, 15]. Their lattice distortion and multi-element synergy can enhance ionic transport while reinforcing the mechanical framework needed for dendrite suppression [16]. In addition to improving bulk electrolyte properties, creating a facile electrolyte-electrode interface remains critical for realizing long-life Li metal batteries [17-20]. One

promising approach can be the in situ polymerization of cyclic ethers such as 1,3-dioxolane (DOL) within the composite separator matrix [20-29]. In situ polymerization can produce a conformal and well-integrated polymer network that ensures intimate contact with the Li metal anode and provides efficient lithium conduit channels in the cathode [30-35]. Furthermore, the use of suitable lithium salts during polymerization can promote the formation of a stable, ionically conductive solid electrolyte interphase on lithium [36, 37]. Different salts contribute distinct functionalities, such as enhancing ionic conductivity, improving interfacial stability, or forming protective inorganic-rich species, that together optimize electrochemical performance [38, 39].

This manuscript presents a study on the design, synthesis, and characterization of a ceramic-polymer composite electrolyte coupled with in situ polymerization, named as HECPE (Polymer: P(VDF-HFP), salt: LiTFSI, ceramic: $Li_{1.3}(AlScY)_{0.3}(ZrTiSn)_{1.7}(PO_4)_3$). It discusses the $LiPF_6$ salt-mediated in situ polymerization of DOL monomer at the electrode interface. To design a robust lithium-ion conductive and stable interphase, LiDFOB, LiFSI, and LiTFSI salts are used. Ultimately, the findings underscore the pivotal role of HECPEs and engineered in situ polymerized interphases in the development of high-performance, safe, and scalable energy storage systems for future applications.

2. Experimental Methodology

A mixture of precursors including lithium hydroxide (LiOH), tin(IV) chloride pentahydrate ($SnCl_4 \cdot 5H_2O$), zirconium oxide (ZrO_2), titanium dioxide (TiO_2), aluminium nitrate nonahydrate ($Al(NO_3)_3 \cdot 9H_2O$), scandium oxide (Sc_2O_3), yttrium oxide (Y_2O_3), and

ammonium dihydrogen phosphate ($NH_4 \cdot H_2PO_4$) was prepared based on stoichiometric proportions. To compensate for the potential volatilization of lithium during high-temperature sintering, an additional 10 wt.% of LiOH was included. The initial mixture was subjected to ball milling for 12 h to ensure homogenization, followed by calcination at 600 °C for 12 h to promote the decomposition of volatile components. After cooling, the powders were milled for an additional 12 h and subsequently dried. The fine powder was then compacted into pellets of 10 mm diameter using a uniaxial pressure of approximately 200 MPa. These green pellets were finally sintered at 1200 °C for 12 h to achieve the desired phase. Then, the pellets were crushed and ball-milled to obtain fine ceramic particles for use as fillers to fabricate ceramic-in-polymer composite electrolytes.

A lithium salt solution of lithium bis(trifluoromethanesulfonyl)imide (LiTFSI, 0.33 M), Lithium bis(fluorosulfonyl)imide (LiFSI, 0.33M), and lithium difluoro(oxalato)borate (LiDFOB, 0.33 M) was prepared by dissolving the salts in 1,3-dioxolane (DOL) monomer under continuous stirring. In parallel, a separate solution containing lithium hexafluorophosphate ($LiPF_6$, 0.2 M) was prepared in 1,2-dimethoxyethane (DME) solvent. The DME-based solution was then added to the DOL-based electrolyte in a 1:4 volume ratio, and the resulting mixture was stirred for 1.5 hours to ensure complete homogeneity. In this formulation, 1,2-dimethoxyethane (DME) served as a plasticizer, promoting enhanced lithium-ion transport, while lithium hexafluorophosphate ($LiPF_6$) acted as an initiator for the in situ polymerization of the 1,3-dioxolane (DOL) monomer. The final electrolyte solution was subsequently utilized to fabricate solid-state lithium cells.

To fabricate the ceramic-in-polymer composite solid electrolyte membranes, a predetermined amount of P(VDF-HFP) polymer and LiTFSI salt were first dissolved in N, N-dimethylformamide (DMF) solvent (weight ratio of polymer to salt is 5:2). Subsequently, 15 wt.% NASICON-type ceramic filler was incorporated into the solution. The resulting viscous mixtures were subjected to vigorous stirring to ensure homogeneity, followed by drop-casting onto glass petri dishes. These membranes were then dried under vacuum at 60 °C for 24 hours, followed by the use of 5 µL liquid monomer-salt solution at the electrodes' interfaces during the coin cell fabrication.

Symmetrical lithium cells (Li|HECPE|Li) were fabricated using lithium metal chips (Lithium metal chips' surface was scraped out and rolled out before use). For the fabrication of symmetrical lithium cells (Li|LECPE|Li), all procedures were followed as for Li|HECPE|Li, except for the addition of LiDFOB and LiFSI salts. Asymmetrical Li|Cu cells were assembled using a lithium metal chip and a copper foil as the electrodes. The cathode slurries of $LiFePO_4$ were prepared using N-methyl-2-pyrrolidone (NMP) as the solvent, and a composite ratio of 80:10:10 for active material, Ketjen black, and PVDF binder, respectively. The slurries were coated onto aluminum foil current collectors and dried under vacuum at 120 °C for 24 hours. Circular cathodes were then punched and transferred into an argon-filled glovebox to fabricate the full-cell (Li|$LiFePO_4$) assembly. After the cell fabrication, the cells were kept at room temperature for 48 h for the polymerization to occur. Figure S1 presents the digital photograph of the HECPE electrolyte before (t = 0 h) and after polymerization (t = 48 h).

The crystallographic structure of the sintered samples was analyzed using X-ray diffraction (XRD) with Cu-Kα radiation over a 2θ range of 10°-60°, and LeBail refinement was conducted using TOPAS (version 6) to confirm the phase [40]. Surface morphology and microstructure were examined using a field emission scanning electron microscope (FE-SEM, JEOL-7610+). Electrochemical impedance spectroscopy (EIS) and DC polarisation measurements were performed with an SP-50e (Biologic) electrochemical workstation over the frequency range of 1 Hz to 1 MHz. Linear sweep voltammetry was carried out in a Keithley Source Meter Unit (model 2450-EC). Galvanostatic charge-discharge (GCD) analysis was done in a Neware CT-2001A battery testing system. All tests, except EIS, were conducted at room temperature (~25 °C).

3. Results and Discussions

The crystalline phase of the synthesized ceramic powder was analyzed through XRD, and the obtained pattern is shown in Figure 1(a). The Le Bail refinement carried out using Topas Academic software (version 6) confirmed the formation of a rhombohedral $R\bar{3}c$ phase. As the literature supports, the high-symmetry rhombohedral phase in NASICON-type lithium-ion solid electrolytes is more favorable for ionic conduction compared to the low-symmetry monoclinic C2/c phase, which generally forms at lower synthesis temperatures [41, 42]. The refined lattice parameters obtained from Le Bail fitting are in good agreement with reported values in our earlier study [17]. The XRD pattern (Figure 1(b)) displayed distinct diffraction peaks corresponding to Rhombohedral

$Li_{1.3}(AlScY)_{0.3}(ZrTiSn)_{1.7}(PO_4)_3$ thereby verifying the successful integration of ceramic filler in the PVDF-HFP/LiTFSI polymer matrix.

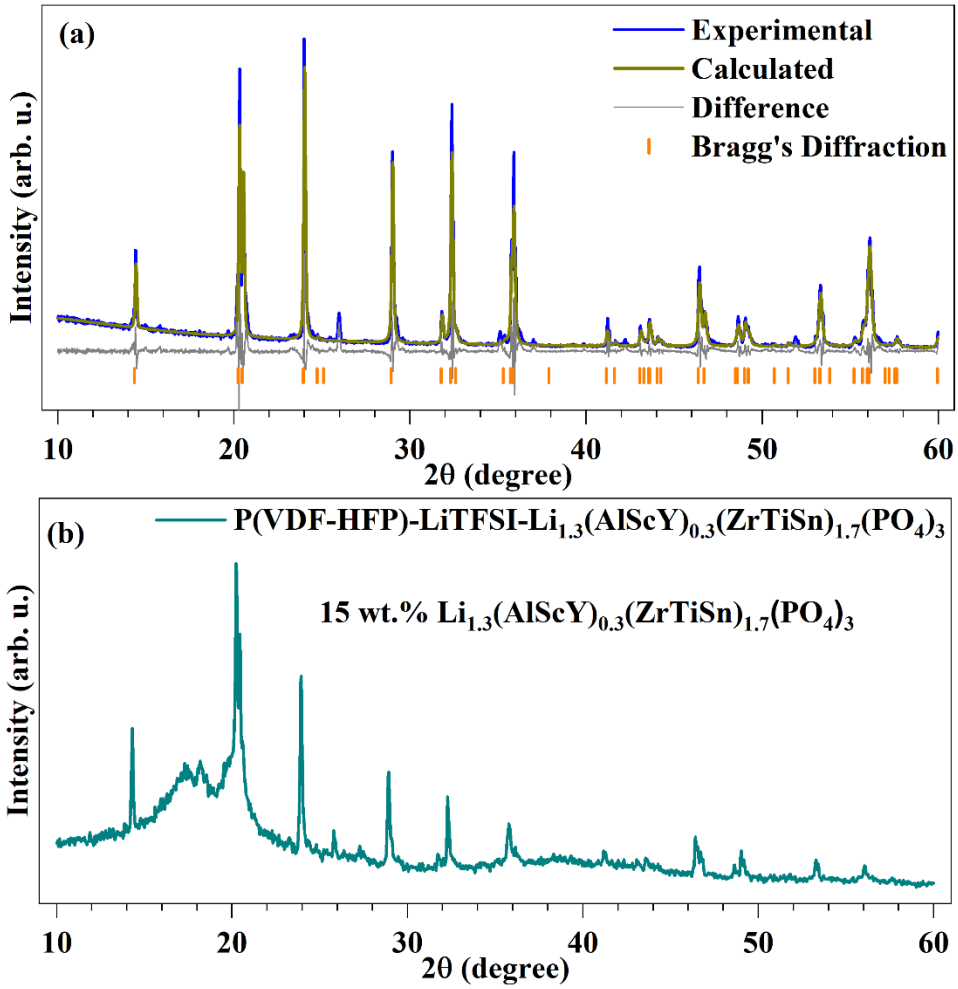

Figure 1:(a) Le-Bail refinement of Room temperature powder X-ray diffraction data for $Li_{1.3}Al_{0.1}Sc_{0.1}Y_{0.1}Sn_{1.7/3}Zr_{1.7/3}Ti_{1.7/3}(PO_4)_3$ sample calcined at 1200 °C for 12 h. (b) The XRD pattern obtained at room temperature for HECPE electrolyte membrane.

Figures 2(a) & 2(b) present the cross-sectional SEM image and EDS elemental mapping of the HECPE electrolyte infused into the LFP cathode, respectively. The SEM image reveals an interfacial polymer layer attached to the surface of the LFP cathode coated on the Al current collector. The EDS mapping confirms the effective infiltration of the polymer electrolyte into the LFP cathode. The elemental mappings of B, F, S, and N come

from the different salts (LiTFSI, LiFSI, LiDFOB, and $LiPF_6$) used in the polymer electrolyte preparation. Importantly, the penetration of HECPE electrolyte in the liquid state into the pores of the LFP cathode establishes continuous Li-ion conductive pathways, which are essential for operating the solid-state battery at higher C-rates.

Figure 3(a) presents the Nyquist plots ($-Z''$ *vs.* Z') of the HECPE sample at different temperatures. The long tail feature at the low-frequency region in the Nyquist plots indicates the ionically insulating nature of the stainless steel (in HECPE). The Nyquist plot was fitted with a series combination of a resistor (R1) and a constant phase element (Q1). The conductivity of the samples was calculated using the dimensions of the sample and the fitted resistance from the Nyquist plot. Further, the conductivity values at different temperatures and the Arrhenius equation (Eq. 1) were used to calculate the activation energy for the ionic motion in the electrolyte samples via linear fitting of ln (σ) with 1000/T, and it was found to be ~ 0.22 eV (Figure 3(b)). The Arrhenius equation is as follows:

$$\sigma(T) = \sigma_0 e^{-\frac{E_A}{k_B T}} \quad (1)$$

where *T:* absolute temperature and k_B: Boltzmann constant, σ_0: pre-exponential factor, and E_A : activation energy.

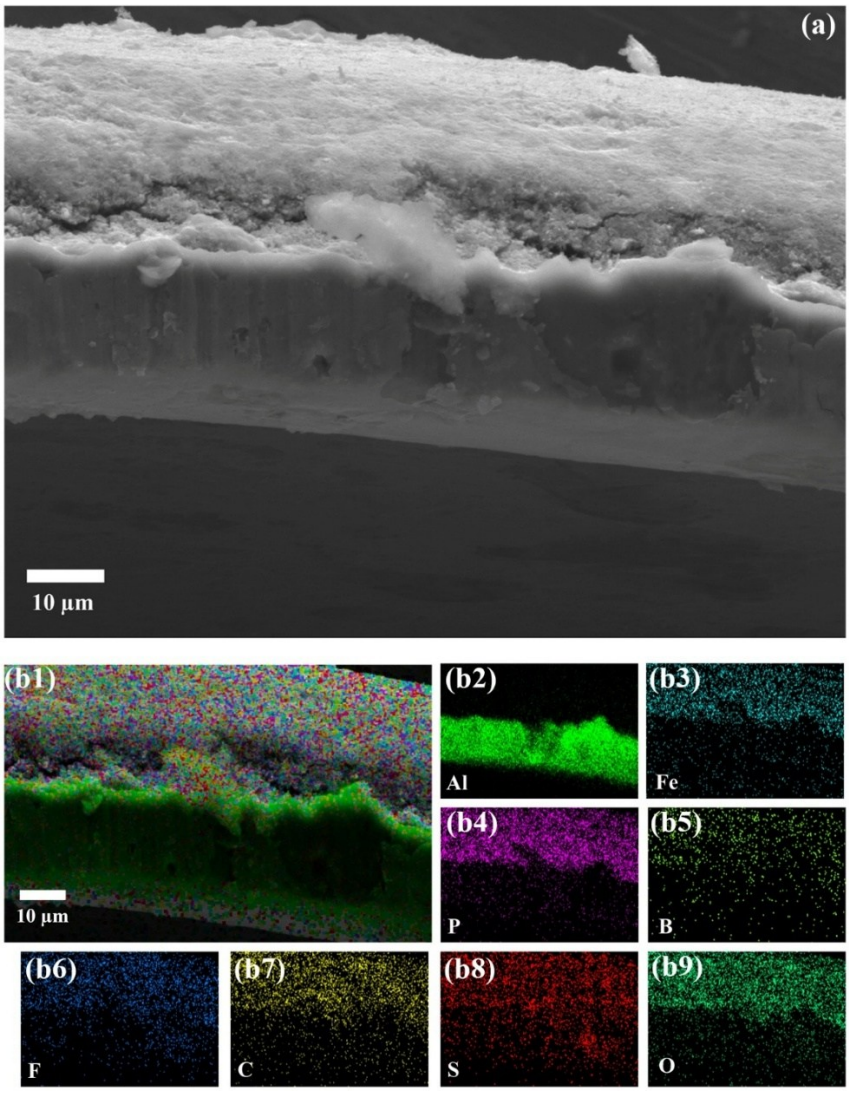

Figure 2: (a) SEM image of the cross-section of the HECPE electrolyte infiltrated into the LFP cathode coated on the Al-current collector. (b1-b9) Different elements' EDS mapping of the cross-section of the HECPE electrolyte infiltrated into the LFP cathode coated on the Al-current collector.

Lithium dendrite formation and coulombic efficiency at higher C-rates are strongly influenced by the lithium-ion transference number (t_{Li+}), since a localized electric field can develop at the electrode surface due to the uneven distribution of anions and cations [43, 44]. The Bruce-Vincent technique, which integrates both direct current (DC) polarization and alternating current (AC) impedance measurements, is commonly employed to evaluate t_{Li+} [45]. For the present study, Li|HECPE|Li symmetric cells were polarized by

applying a DC potential of 10 mV for 3 h, after which the current stabilized without further significant change. Before DC polarization, electrochemical impedance spectroscopy (EIS) with a 10 mV AC perturbation was performed to determine the initial interfacial resistance (R_0) of the cell. Upon applying the DC bias, both ions and electronic motion contributed to the initial current (I_0) at t = 0 h. The initial current (I_0) was calculated using the formula $I_0 = \Delta V/(R_{bulk} + R_{ss})$ [46]. Over time, the current decreased due to anion blocking at the lithium electrode surface and the formation of a counter-electrostatic field against the applied potential. At steady state (t = 3 h), the current (I_{SS}) was primarily due to lithium ions migrating through the electrolyte. EIS performed after polarization test provided the steady-state interfacial resistance (R_{SS}).

The evolution of current during polarization in Li | HECPE | Li cells is presented in Figure 3(c), with the inset showing Nyquist plots at t = 0 h and t = 3 h, fitted with the equivalent circuit. The high-frequency intercept corresponds to the electrolyte resistance, while the low-frequency intercept gives the total resistance of the cell. The difference between the two provides the interfacial resistance, which increased from 177 Ω to 190 Ω after polarization, while the bulk resistance of HECPE remained nearly constant. The lithium transference number was calculated to be ~ 0.41 using Eq. (2):

$$t_{Li^+} = \frac{I_{ss}(\Delta V - I_0 R_0)}{I_0(\Delta V - I_{ss} R_{ss})} \quad (2)$$

The high lithium-ion transfer number would help in guiding uniform lithium deposition/dissolution from the lithium metal interface and would increase the critical current density.

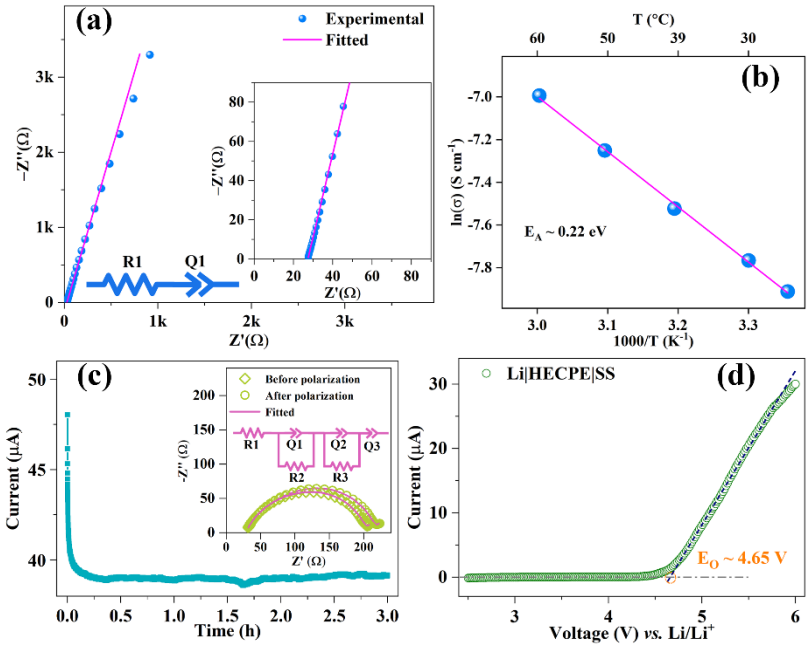

Figure 3: (a) Nyquist plot of in situ polymerised HECPE electrolyte at room temperature. (b) Linear fitting of the temperature-dependent conductivity of the HECPE sample using the Arrhenius equation. (c) Current variation with time upon applying 0.01 V on a symmetric Li | HECPE | Li cell at room temperature. The inset shows the Nyquist plots of the cell at t = 0 h & t = 3 h with the equivalent circuit used to fit the data. (d) Linear sweep voltammetry curves for Li | HECPE | SS at 0.1 mV s^{-1} at room temperature.

Figure 3(d) shows the linear sweep voltammetry (LSV) curve of the Li | HECPE | SS cell measured in the 2.5-6 V range at a scan rate of 0.1 mV s^{-1}. A steep rise in current was observed at ~4.65 V, corresponding to the onset of electrolyte oxidation, limiting its upper voltage window. The high oxidation stability of HECPE can be attributed to Lewis acid–base interactions between the ceramic fillers and the functional groups of the P(VDF-HFP)–LiTFSI matrix, as well as the addition of different salts in the PDOL electrolyte, which suppresses the oxidative decomposition of the polymer. Such oxidative robustness renders HECPE suitable for application with high-voltage cathode materials, including spinel-type and layered oxides, thereby extending its potential use in advanced all-solid-state lithium batteries.

The electrochemical properties of HECPE were evaluated by assembling both symmetric and full cells to assess its practical performance in solid-state lithium batteries. For the symmetric cell studies, the configuration consisted of lithium metal chips placed on both sides of the HECPE solid electrolyte membrane. As depicted in Figure 4(a), the symmetric Li | HECPE | Li cell was subjected to lithium plating-stripping at various current densities to determine its critical current density (CCD) up to which the solid-state electrolyte can operate stably. At low current densities, the HECPE cell maintained a nearly constant overpotential, indicating uniform lithium deposition and dissolution at the Li-electrolyte interface. However, as the current density increased, the cell exhibited a progressive rise in polarization, and the voltage profiles transitioned to a sloped shape, indicative of increased ion transport resistance and possible inhomogeneous Li deposition. Considering the electrical integrity fact, the HECPE-based symmetric cell could sustain its electrical integrity up to 4 mA cm^{-2}, which is notably high for a polymer-based solid electrolyte. However, the corresponding high overpotential ~1.5 V at 4 mA cm^{-2} is impractical for real-world battery applications due to the lower and upper limit of the operational voltage window. Further, the overpotential curves at 1 mA cm^{-2} seem to follow a steady overpotential value with time, unlike for 4 mA cm^{-2}, where there is a rapid increase in the overpotential value with time. Accordingly, while the electrolyte can withstand high currents (up to 4 mA cm^{-2}) without immediate failure, the critical current density for practical battery applications with acceptable performance and efficiency is only ~1 mA cm^{-2}.

To further assess the long-term cycling durability of the HECPE electrolyte, galvanostatic charge-discharge cycling was performed for 3000 cycles at a moderate current density of 0.2 mA cm^{-2}, as shown in Figure 4(b). Impressively, the cell demonstrated highly stable cycling with negligible polarization growth and no evidence of soft (noisy overpotential curves) or hard short-circuiting (Fully flat overpotential curves) throughout the testing period. The nearly invariant overpotential across cycles and minimal drift indicate uniform Li plating/stripping and the presence of a stable Li-electrolyte interphase. Further, Li|Li symmetric cells were tested at a high current density of 1 mA cm^{-2} (Figures S2 and S3). The results showed that the symmetric cell with the HECPE electrolyte system outperforms the LECPE electrolyte system in terms of uniform and stable lithium plating-stripping, due to the presence of different salts. LiTFSI is known to have a high ionic conductivity. LiDFOB and LiFSI salts facilitate the formation of a stable, ionically conductive solid electrolyte interphase (SEI) on the lithium surface, thereby guiding uniform lithium plating/stripping over a long period. Further, the Li|Cu cells were tested to assess the lithium plating-stripping efficiency of our HECPE electrolyte system at a current density of 1 mA cm^{-2}, with a plating capacity of ~ 1 mAh cm^{-2}, for long-term cyclability (Figure S4). Initially, the columbic efficiency was low, but it improved to ~ 95% on cycling. This remarkable cycling stability highlights the outstanding durability of the HECPE electrolyte, making it a promising candidate for practical solid-state lithium battery applications.

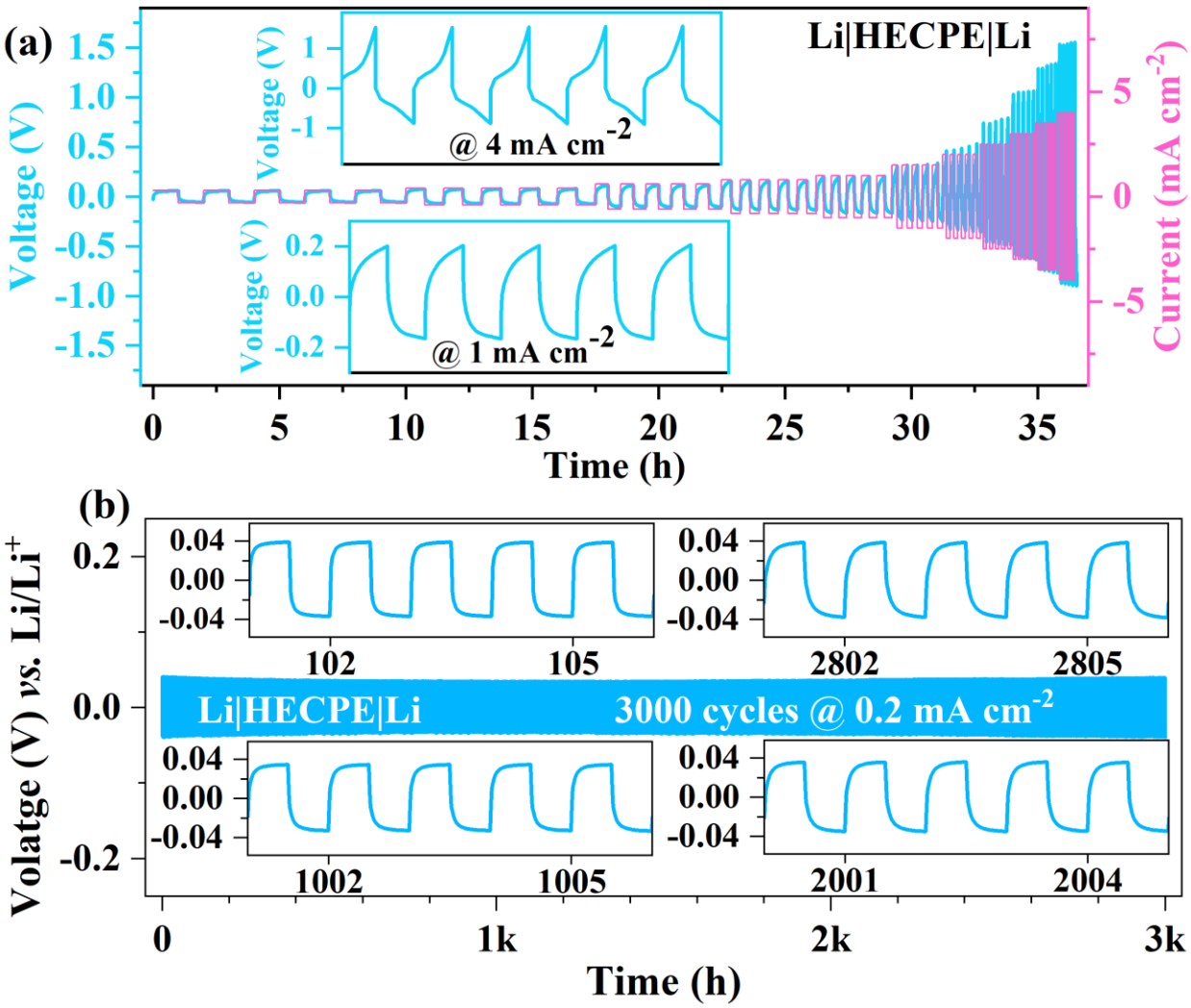

Figure 4: (a) The room temperature galvanostatic polarization curves indicate lithium plating-stripping in Li | HECPE | Li cell at different current densities. (b) Long-term lithium plating-stripping polarisation curves at 0.2 mA cm^{-2} at room temperature.

The electrochemical performance of full cells employing the HECPE electrolyte was assessed using olivine-structured $LiFePO_4$ (LFP) cathode paired with a lithium metal anode. Figure 5(a) shows that at a current density equivalent to 0.2C (1C is 170 mA g^{-1}), the LFP cathode delivered a high discharge capacity of approximately 158 mAh g^{-1} at room temperature. As the current density increased, the room temperature discharge

capacity declined to ~139 mAh g^{-1}, 92 mAh g^{-1}, and 32 mAh g^{-1} at 0.5C, 1C, and 2C, respectively.

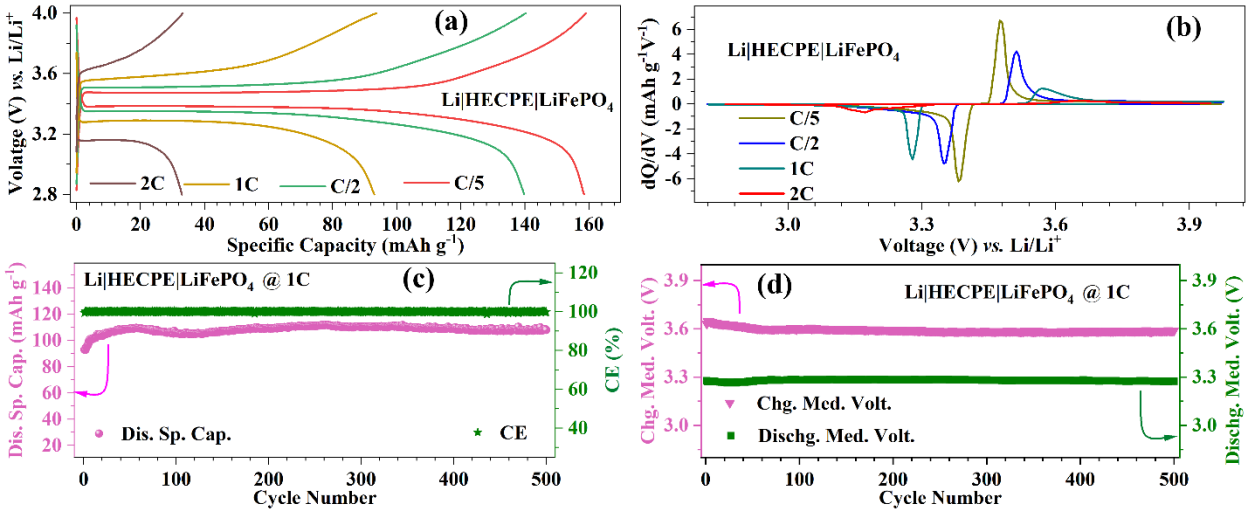

Figure 5: (a) Room temperature specific capacity-voltage curves at different C-rates of Li | HECPE | $LiFePO_4$ cells. (b) Room temperature differential capacity vs. Voltage (dQ/dV vs V) curves at different C-rates of Li | HECPE | $LiFePO_4$ cells. (c) Room temperature long-term cycling data of Li | HECPE | $LiFePO_4$ cells at 1C. (d) Room temperature long-term behavior of median charging and discharging voltages of Li | HECPE | $LiFePO_4$ cells cycling at 1C.

Also, this capacity fading at higher C-rates was accompanied by an increase in polarization potential, as shown in the dQ/dV (differential capacity) vs. V curves at different C-rates (Figure 5(b)), resulting in a decrease in energy efficiency. Although the in situ polymerization process effectively provided sufficient ion transport pathways both at the interfaces and the cathode bulk, the high polarization potential and low discharge specific capacity are primarily attributed to the limited Li^+ diffusion kinetics within the cathode particles. Remarkably, when the LFP cells are cycled at 1C for 500 cycles, there is an increase in the discharge specific capacity to 111 mAh g^{-1} at the 262nd cycle (Figure 5(c)), which then reduces to 107 mAh g^{-1} at the 500th cycle with a steady coulombic efficiency of ~ 99.9%. The slight capacity increase observed in the initial cycles

of Fig. 5c is attributed to electrochemical conditioning and progressive interfacial optimization during early cycles. Initial cycles promote improved wetting and mechanical settling of the HECPE into electrode pores, and gradual activation of continuous Li^+ conduction pathways in the cathode. Further, the variation in cell charge and discharge voltages with cycling indicates the high polarization (difference between the charge median voltage and discharge median voltage, Figure 5(d)) in initial cycles, which gets stabilized with a reduced value on further cycling. These results indicate that initially, there was a formation of stable interphase at both the anode and the cathode sides, which guided uniform and efficient Li^+ conduction with cycling. The high cyclability is attributed to several key factors: (i) the inherently small volume change during Li^+ intercalation/de-intercalation in LFP, aided by the rigid PO_4 tetrahedral framework bridging FeO_6 octahedra; (ii) the electrochemical stability of the HECPE electrolyte within the operating voltage range of LFP; (iii) its excellent compatibility with lithium metal, enabling the formation of a stable passivation layer; and (iv) the development of a robust cathode–electrolyte interphase (CEI). Table S1 presents a comparison of our work with relevant studies in terms of conductivity, Lithium plating-stripping cyclability, and long-term full cell cyclability using $LiFePO_4$ as the cathode material. The stable electrode-electrolyte interfaces endowed the Li|HECPE|Li cells and LFP|HECPE|Li cell with excellent electrochemical stability, high coulombic efficiency, and prolonged cycling performance, demonstrating its strong potential for practical solid-state lithium battery applications.

4. Conclusions

In this work, we demonstrated a multifunctional solid-state electrolyte architecture (HECPE) that combines a high-entropy ceramic-in-polymer composite with an in situ polymerized poly(1,3-dioxolane) containing multiple lithium salts (LiTFSI, LiFSI, and LiDFOB). The synergistic salt strategy effectively modulated the interfacial chemistry at the lithium metal surface, enabling uniform Li plating/stripping and achieving a high critical current density of ~1 mA cm^{-2}. The HECPE framework provided ~ 4.65 V as a limit upper electrochemical voltage window and a lithium-ion transference number (~0.41). Electrochemical evaluation revealed that Li|LFP full cells with HECPE electrolytes delivered high discharge capacity, excellent rate performance at moderate C-rates, and remarkable long-term cycling stability over 500 cycles with nearly invariant Coulombic efficiency. Overall, the integration of high-entropy NASICON-type fillers with an in situ polymerized PDOL electrolyte and multi-salt chemistry establishes an efficient dynamic ion transport network and robust electrode–electrolyte interfaces. This study presents a viable pathway for developing safe, scalable, and high-performance solid-state lithium metal batteries with extended cycle life and compatibility with LFP cathode.

Conflicts of Interest

There are no conflicts of interest to declare.

Data Availability Statement

The data that support the findings of this study are available from the corresponding authors upon reasonable request.

Credit author statement

Asish Kumar Das: Conceptualisation, Methodology, Investigation, Funding acquisition, Data curation, Formal analysis, Writing - Original Draft; **Sunil Kumar:** Funding acquisition, Supervision, Resources, Project administration, Validation, Writing - Review & Editing.

Acknowledgments

The author (AKD) thanks the Ministry of Education, Government of India, for the Prime Minister's Research Fellowship (PMRF) (PMRF ID - 2102737). The authors gratefully acknowledge the Ministry of Education (MoE), Government of India (Grant No. MoE-STARS/STARS-2/2023-0365).

Supporting Information

Digital photographs demonstrating the HECPE before and after polymerization; lithium plating-stripping results of Li | HECPE | Li and Li | LECPE | Li cells at high current density; coulombic efficiency of Li | Cu cell; a comparison table of the results with various works.

References

(1) Winter, M.; Barnett, B.; Xu, K. Before Li Ion Batteries. *Chem. Rev.* **2018**, *118* (23), 11433. DOI: https://doi.org/10.1021/acs.chemrev.8b00422.

(2) Megahed, S.; Ebner, W. Lithium-ion battery for electronic applications. *J. Power Sources* **1995**, *54* (1), 155. DOI: https://doi.org/10.1016/0378-7753(94)02059-C.

(3) Chen, F.; Yang, D.; Zha, W.; Zhu, B.; Zhang, Y.; Li, J.; Gu, Y.; Shen, Q.; Zhang, L.; Sadoway, D. R. Solid polymer electrolytes incorporating cubic $Li_7La_3Zr_2O_{12}$ for all-solid-state lithium rechargeable batteries. *Electrochim. Acta* **2017**, *258*, 1106. DOI: https://doi.org/10.1016/j.electacta.2017.11.164.

(4) Goodenough, J. B.; Park, K.-S. The Li-Ion Rechargeable Battery: A Perspective. *J. Am. Chem. Soc.* **2013**, *135* (4), 1167. DOI: https://doi.org/10.1021/ja3091438.

(5) Diouf, B.; Pode, R. Potential of lithium-ion batteries in renewable energy. *Renew. Energ.* **2015**, *76*, 375. DOI: https://doi.org/10.1016/j.renene.2014.11.058.

(6) Cheng, X.-B.; Zhang, R.; Zhao, C.-Z.; Zhang, Q. Toward Safe Lithium Metal Anode in Rechargeable Batteries: A Review. *Chem. Rev.* **2017**, *117* (15), 10403. DOI: https://doi.org/10.1021/acs.chemrev.7b00115.

(7) Schmuch, R.; Wagner, R.; Hörpel, G.; Placke, T.; Winter, M. Performance and cost of materials for lithium-based rechargeable automotive batteries. *Nat. Energy* **2018**, *3* (4), 267. DOI: https://doi.org/10.1038/s41560-018-0107-2.

(8) Grey, C. P.; Hall, D. S. Prospects for lithium-ion batteries and beyond—a 2030 vision. *Nat. Commun.* **2020**, *11* (1), 6279. DOI: https://doi.org/10.1038/s41467-020-19991-4.

(9) Evarts, E. C. Lithium batteries: To the limits of lithium. *Nature* **2015**, *526* (7575), S93. DOI: https://doi.org/10.1038/526S93a.

(10) Das, A. K.; Badole, M.; Vasavan, H. N.; Saxena, S.; Gami, P.; Kumar, S. Highly conductive ceramic-in-polymer composite electrolyte enabling superior electrochemical performance for all-solid-state lithium batteries. *Ceram. Int.* **2023**, *49* (18), 29719, Article. DOI: https://doi.org/10.1016/j.ceramint.2023.06.214.

(11) Das, A. K.; Badole, M.; Vasavan, H. N.; Saxena, S.; Gami, P.; Deswal, S.; Kumar, P.; Kumar, S. Enhancing room temperature performance of solid-state lithium cell via a facile solid electrolyte-cathode interface design. *Mater. Today Sustain.* **2024**, *26*. DOI: https://doi.org/10.1016/j.mtsust.2024.100758.

(12) Das, A. K.; Badole, M.; Vasavan, H. N.; Saxena, S.; Gami, P.; Dagar, N.; Kumar, S. LiTa2PO8-Based Polymer-Ceramic Electrolyte Paved the Way to High-Performance Solid-State Lithium Metal Batteries. *Energy Fuels* **2024**, *38* (12), 11253-11261, Article. DOI: https://doi.org/10.1021/acs.energyfuels.4c01520.

(13) Das, A. K.; Badole, M.; Vasavan, H. N.; Saxena, S.; Gami, P.; Dagar, N.; Kumar, S. Integrated cathode-electrolyte ($Li_{6.55}La_3Zr_{1.55}Ta_{0.45}O_{12}$/PEO-LiTFSI) architecture driven excellent performance of solid-state lithium metal batteries. *J. Energy Storage* **2024**, *94*, Article. DOI: https://doi.org/10.1016/j.est.2024.112452.

(14) Zeng, Y.; Ouyang, B.; Liu, J.; Byeon, Y.-W.; Cai, Z.; Miara, L. J.; Wang, Y.; Ceder, G. High-entropy mechanism to boost ionic conductivity. *Science* **2022**, *378* (6626), 1320. DOI: https://doi.org/10.1126/science.abq1346.

(15) Chen, Y.; Wang, T.; Chen, H.; Kan, W. H.; Yin, W.; Song, Z.; Wang, C.; Ma, J.; Luo, W.; Huang, Y. Local structural features of medium-entropy garnet with ultra-long cycle life. *Matter* **2023**, *6* (5), 1530-1541. DOI: https://doi.org/10.1016/j.matt.2023.03.002.

(16) Feng, Y.; Yang, L.; Yan, Z.; Zuo, D.; Zhu, Z.; Zeng, L.; Zhu, Y.; Wan, J. Discovery of high entropy garnet solid-state electrolytes via ultrafast synthesis. *Energy Storage Mater.* **2023**, *63*, 103053. DOI: https://doi.org/10.1016/j.ensm.2023.103053.

(17) Das, A. K.; Gami, P.; Vasavan, H. N.; Saxena, S.; Dagar, N.; Deswal, S.; Kumar, P.; Kumar, S. Advancing High-Energy Solid-State Batteries with High-Entropy NASICON-type Solid Electrolytes. *ACS Appl. Energy Mater.* **2024**, *7* (19), 8301-8307, Article. DOI: https://doi.org/10.1021/acsaem.4c02011.

(18) Das, A. K.; Kumar, S. Compositionally Tuned High-Entropy Li-Garnet Electrolyte for Advanced Solid-State Batteries. *Batter. Supercaps 0* (n/a), e202500358. DOI: https://doi.org/10.1002/batt.202500358.

(19) Cao, J. H.; Zhang, P.; Wang, Y. K.; Wu, D. Y. Synergistic Dual Electrolyte System of LATP and In- Situ Solod-State PDOL System and its Improvement on the Performance of NCM811 Batteries. *Batter. Supercaps* **2025**, *8* (3), Article. DOI: https://doi.org/10.1002/batt.202400463.

(20) Yang, X.; Sun, C.; Li, R.; Pei, N.; Li, X.; Deng, Y.; Zhang, P.; Lin, J.; Zhao, J. Percolating dynamic ion-conduction network in composite polymer electrolyte for high-performance lithium metal batteries. *Chem. Eng. J.* **2025**, *520*, Article. DOI: https://doi.org/10.1016/j.cej.2025.165754.

(21) Wu, M.; Li, X.; Mei, X.; Zhang, Y.; Zhang, J.; Zheng, C.; Xue, J.-P.; Zhou, L. In Situ Polymerization of 1,3-Dioxane in Solid-State Lithium Batteries: A Mini-Review of Recent Developments. *Energy & Fuels* **2025**, *39* (27), 12830-12846. DOI: https://doi.org/10.1021/acs.energyfuels.5c01954.

(22) Zhang, W.; Tian, W.; Chen, X.; Ma, S.; Chen, X.; Li, Q.; Liu, Y.; Wu, X.; Wen, Z.; Wu, Y.; et al. Construction of self-supporting PDOL electrolyte membranes for stable solid-state lithium metal batteries. *J. Colloid Interface Sci.* **2025**, *699*, Article. DOI: https://doi.org/10.1016/j.jcis.2025.138224.

(23) Cao, J.; Zhang, M.; Xu, J.; Wang, M.; Hong, B.; Lai, Y. The Manipulation of Ring-Open Polymerization Process to Boost the Electrochemical Performance for Solid-State Lithium Metal Batteries. *ChemSusChem* **2025**, *18* (8), Article. DOI: https://doi.org/10.1002/cssc.202402028.

(24) Gao, H.; Zhou, Y.; Wang, K.; Li, B.; Wang, S.; Li, W.; Nai, J.; Liu, Y.; Wang, Y.; Zou, S. An In Situ Polymerized Solid-State Electrolyte for Uniform Lithium Deposition via the Piezoelectric Effects. *Adv. Energy Mater.* **2025**, *15* (28), Article. DOI: https://doi.org/10.1002/aenm.202501379.

(25) Li, S.; Hong, H.; Yang, X.; Li, D.; Xiong, Q.; Zhang, D.; Wang, S.; Huang, Z.; Lv, H.; Zhi, C. In Situ Polymerized Polyfluorinated Crosslinked Polyether Electrolytes for High-Voltage Lithium Metal Batteries. *Adv. Mater.* **2025**, *37* (29), Article. DOI: https://doi.org/10.1002/adma.202504333.

(26) Li, X.; Yang, X.; Li, R.; Lai, P.; Chen, M.; Li, W.; Chen, Q.; Deng, Y.; Zhang, P.; Zhao, J. Multiscale Collaborative Optimization for Composite Solid Electrolyte to Achieve High-Performance Lithium Metal Batteries. *Small* **2025**, *21* (10), Article. DOI: https://doi.org/10.1002/smll.202412054.

(27) Zhang, W.; Tian, W.; Chen, X.; Ma, S.; Chen, X.; Li, Q.; Liu, Y.; Wu, X.; Wen, Z.; Wu, Y. Construction of self-supporting PDOL electrolyte membranes for stable solid-state lithium metal batteries. *J. Colloid Interface Sci.* **2025**, *699*, Article. DOI: https://doi.org/10.1016/j.jcis.2025.138224.

(28) Tang, W.; Zhou, T.; Duan, Y.; Zhou, M.; Li, Z.; Liu, R. Nonflammable in situ PDOL-based gel polymer electrolyte for high-energy-density and high safety lithium metal batteries. *Carbon Neutralization* **2024**, *3* (3), 386-395. DOI: https://doi.org/10.1002/cnl2.130.

(29) Li, Z.; Tang, W.; Deng, Y.; Zhou, M.; Wang, X.; Liu, R.; Wang, C.-a. Enabling highly stable lithium metal batteries by using dual-function additive catalyzed in-built quasi-solid-state polymer electrolytes. *J. Mater. Chem. A* **2022**, *10* (43), 23047-23057, 10.1039/D2TA06153H. DOI: https://doi.org/10.1039/D2TA06153H.

(30) Wang, C.; Xia, Z.; Bai, G.; Li, D.; Wang, C.; Zhou, X.; Zhang, T.; Liu, X. Thermoplastic polyurethane reinforced in-situ polymerization polymer/Li6.75La3Zr1.75Ta0.25O12 composite solid electrolyte for solid-state lithium batteries. *J. Energy Storage* **2025**, *132*, Article. DOI: https://doi.org/10.1016/j.est.2025.117730.

(31) Wang, Z.; Wang, J.; Liao, Y.; Lin, Z. In-situ polymerization of poly(1,3-dioxolane) gel electrolytes modified with LLZTO nanoparticles for high-performance lithium-metal batteries. *Electrochim. Acta* **2025**, *513*, Article. DOI: https://doi.org/10.1016/j.electacta.2024.145593.

(32) Zhu, T.; Wang, G.; Hou, J.; Sun, W.; Song, C.; Yuan, Q.; Zhang, C.; Lei, X.; Su, Y.; Chen, M. Heterogeneous Engineered Solid Electrolyte for Seamless and Stable Integration of Anode and Cathode. *Adv. Funct. Mater.* **2025**, *35* (29), Article. DOI: https://doi.org/10.1002/adfm.202501870.

(33) Gao, H.; Zhou, Y.; Wang, K.; Li, B.; Wang, S.; Li, W.; Nai, J.; Liu, Y.; Wang, Y.; Zou, S.; et al. An In Situ Polymerized Solid-State Electrolyte for Uniform Lithium Deposition via the Piezoelectric Effects. *Adv. Energy Mater.* **2025**, *15* (28), 2501379. DOI: https://doi.org/10.1002/aenm.202501379.

(34) Li, Z.; Liu, Q.; Deng, Y.; Zhou, M.; Tang, W.; Dong, H.; Zhao, W.; Liu, R. In situ cross-linked plastic crystal electrolytes toward superior lithium metal batteries. *Mater. Today Energy* **2023**, *31*, 101198. DOI: https://doi.org/10.1016/j.mtener.2022.101198.

(35) Wang, M.; Zhang, H.; Li, Y.; Liu, R.; Yang, H. A three-dimensional co-continuous network structure polymer electrolyte with efficient ion transport channels enabling ultralong-life all solid-state lithium metal batteries. *J. Energy Chem.* **2024**, *94*, 635-645. DOI: https://doi.org/10.1016/j.jechem.2024.02.069.

(36) Sun, Z.; Yang, J.; Wu, Y.; Meng, F.; Niu, Y.; Xu, H.; Zhu, Y.; Hong, B.; Chen, Z.; Zhu, J. Stabilizing Residual Monomers within In Situ Polymerized Electrolytes for High-Voltage Lithium Metal Batteries. *J. Am. Chem. Soc.* **2025**, *147* (21), 18064-18073, Article. DOI: https://doi.org/10.1021/jacs.5c03911.

(37) Yang, S.; Yan, J.; Chou, J.; Zhang, H.; Wang, Z.; Guo, H.; Li, X.; Yan, G.; Peng, W.; Li, G.; et al. High Li+ Coordination Entropy Reducing the Interaction between Li+ and Polymer Chains to Improve Li+ Transport for Solid-State Lithium Metal Batteries. *Adv. Funct. Mater. 35* (38), 2502741. DOI: https://doi.org/10.1002/adfm.202502741.

(38) Pan, Q.; Yang, W.; Wu, C.; Xie, D.; Wang, Y. Poly(1,3-Dioxolane)-Modified $Li_{1.3}Al_{0.3}Ti_{1.7}(PO_4)_3$ as the Electrolyte for Enhanced Solid Lithium Metal Batteries. *Chem. Eur. J.* **2025**, *31* (12), Article. DOI: https://doi.org/10.1002/chem.202403915.

(39) Wu, M.; Li, X.; Zhang, Y.; Mei, X.; Shen, F.; Zheng, C.; Xue, J. P.; Zhou, L. In-Situ Polymerization of 1,3-Dioxane Driven by a Bifunctional Initiator as Polymer Electrolytes for High Performance Solid-State Lithium Metal Batteries. *ACS Appl. Energy Mater.* **2025**, *8* (15), 11749-11757, Article. DOI: https://doi.org/10.1021/acsaem.5c01965.

(40) Coelho, A. TOPAS and TOPAS-Academic: an optimization program integrating computer algebra and crystallographic objects written in C++. *J. Appl. Crystallogr.* **2018**, *51* (1), 210. DOI: https://doi.org/10.1107/S1600576718000183.

(41) Gami, P.; Badole, M.; Vasavan, H. N.; Das, A. K.; Saxena, S.; Dagar, N.; Srihari, V.; Kumar, S. NASICON-type medium entropy $Li_{1.5}Sn_{1.0}Al_{0.5}Zr_{0.5}(PO_4)_3$ electrolyte for solid state Li metal batteries. *J. Power Sources* **2024**, *618*, Article. DOI: https://doi.org/10.1016/j.jpowsour.2024.235214.

(42) Gami, P.; Das, A. K.; Badole, M.; Vasavan, H. N.; Saxena, S.; Dagar, N.; Deswal, S.; Kumar, P.; Dwivedi, A.; Poswal, H. K.; et al. Fostering Li-ion conduction in Zr-Sn-Al-based mid-entropy NASICON electrolyte. *Ceram. Int.* **2024**, *50* (22), 47612-47619, Article. DOI: https://doi.org/10.1016/j.ceramint.2024.09.107.

(43) Rosso, M.; Gobron, T.; Brissot, C.; Chazalviel, J. N.; Lascaud, S. Onset of dendritic growth in lithium/polymer cells. *J. Power Sources* **2001**, *97-98*, 804-806. DOI: https://doi.org/10.1016/S0378-7753(01)00734-0.

(44) Chazalviel, J. N. Electrochemical aspects of the generation of ramified metallic electrodeposits. *Physical Review A* **1990**, *42* (12), 7355-7367. DOI: https://doi.org/10.1103/PhysRevA.42.7355.

(45) Evans, J.; Vincent, C. A.; Bruce, P. G. Electrochemical measurement of transference numbers in polymer electrolytes. *Polymer* **1987**, *28* (13), 2324. DOI: https://doi.org/10.1016/0032-3861(87)90394-6.

(46) Lin, L.-Y.; Chen, C.-C. Accurate characterization of transference numbers in electrolyte systems. *J. Power Sources* **2024**, *603*, 234236. DOI: https://doi.org/10.1016/j.jpowsour.2024.234236.

[TOC]

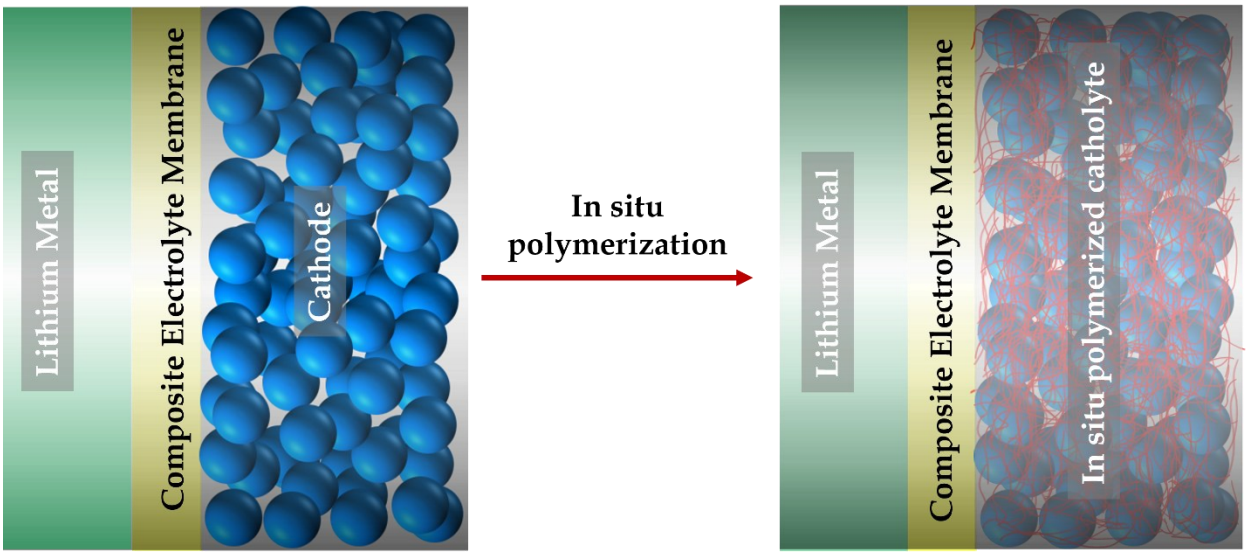
Lithium Metal
Composite Electrolyte Membrane
Cathode
In situ
polymerization
Lithium Metal
Composite Electrolyte Membrane
In situ polymerized catholyte

[Supporting Information]

In Situ Polymerization-Enabled Facile Electrode Interface in Solid-State Lithium-Metal Battery

Asish Kumar Das* and Sunil Kumar**

Department of Metallurgical Engineering and Materials Science, Indian Institute of Technology Indore, Simrol, 453552, India

Corresponding authors E-mail: *phd2201105011@iiti.ac.in, ** sunil@iiti.ac.in

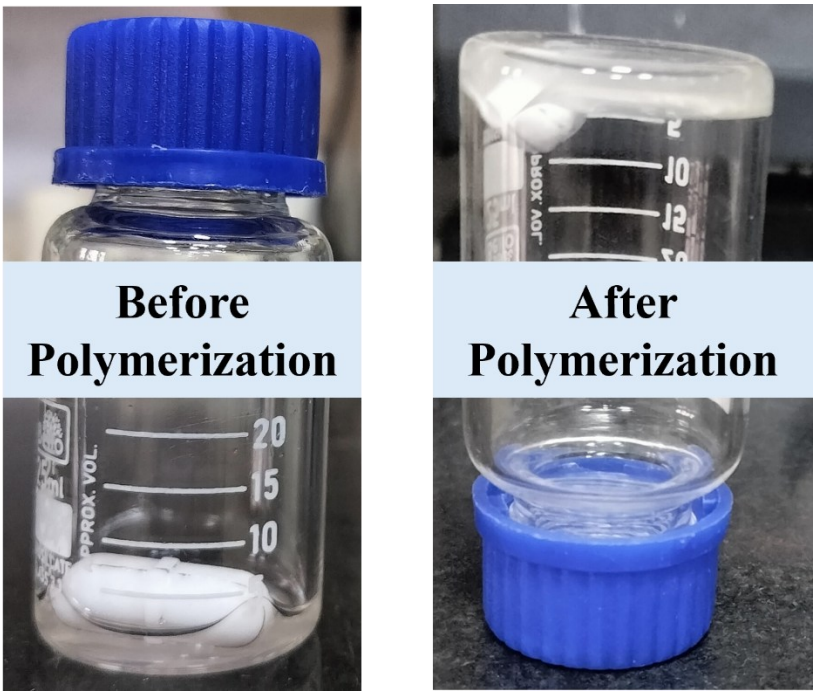

Figure S4: Digital photographs demonstrating the HECPE before and after polymerization.

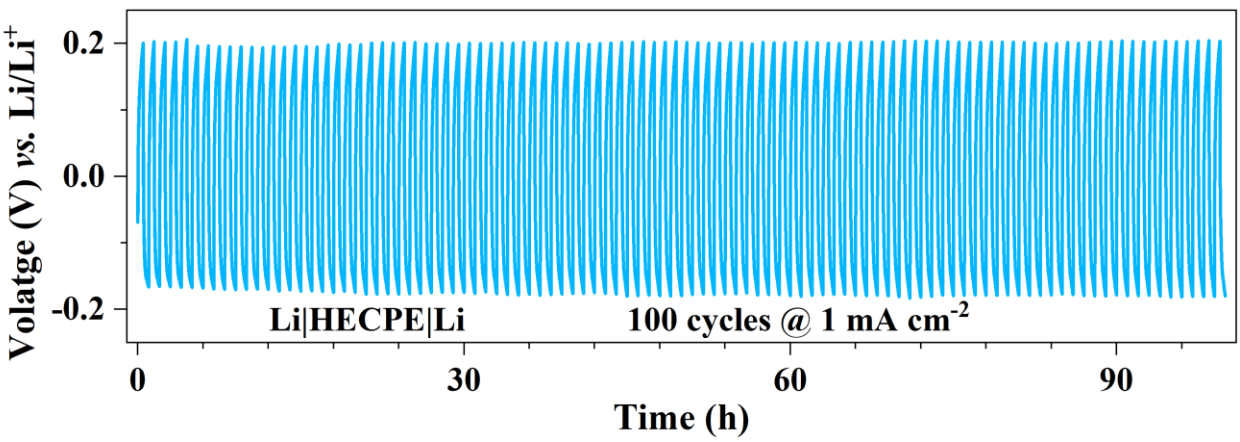

Figure S5: Lithium plating-stripping polarisation curves of Li | HECPE | Li cell at 1 mA cm^{-2} at room temperature.

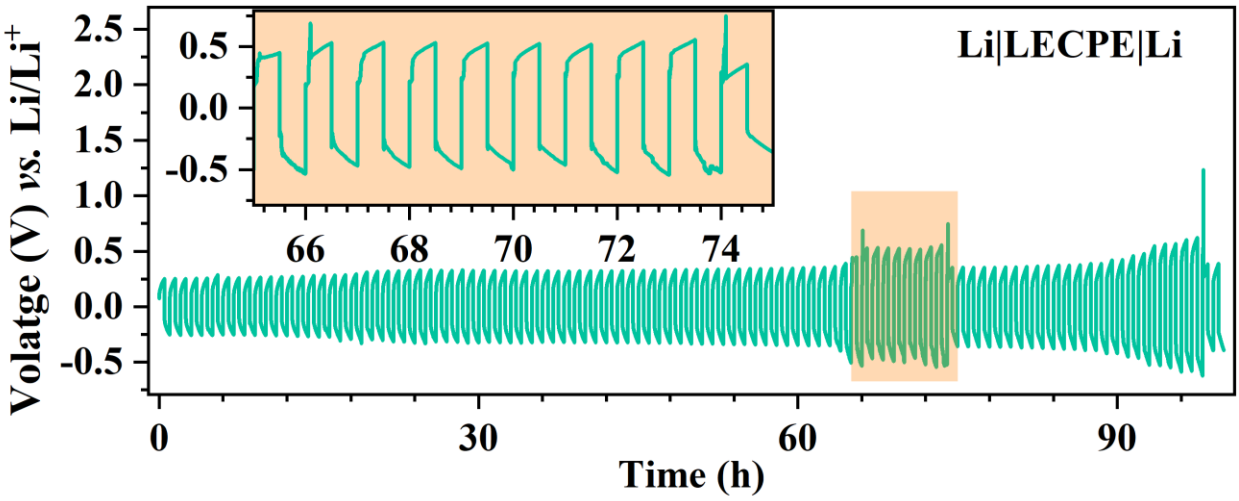

Figure S6: Lithium plating-stripping polarisation curves of Li | LECPE | Li cell at 1 mA cm^{-2} at room temperature.

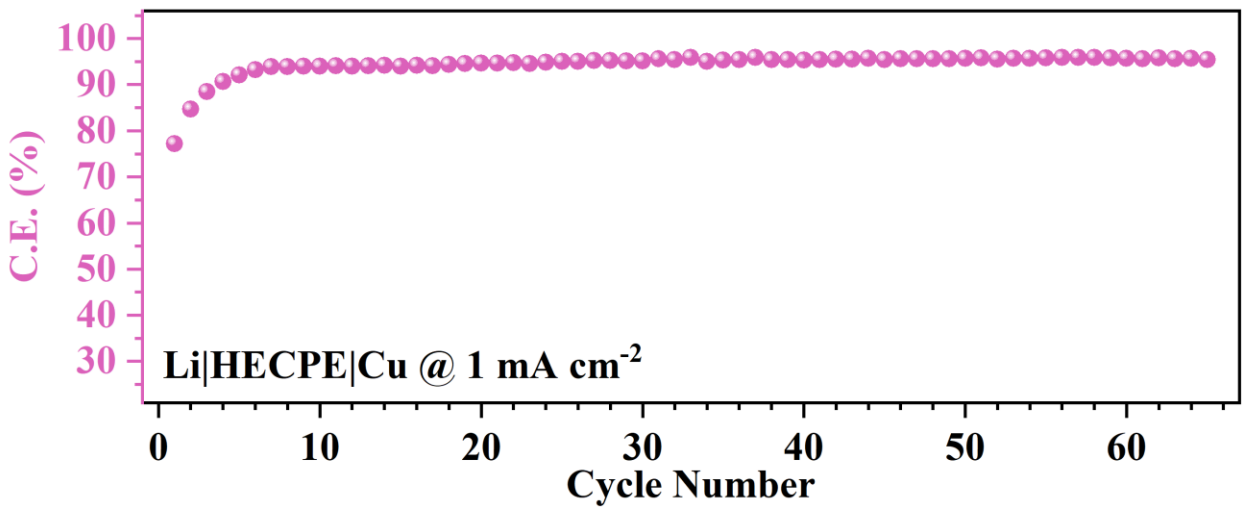

Figure S7: Columbic efficiency of Li | HECPE | Cu cells at 1 mA cm^{-2} (plating capacity of 1 mAh cm^{-2}) at room temperature.

Table S1: Comparison table showing conductivity, Li-Li plating/stripping cyclability, and Li-$LiFePO_4$ full cell's cyclability with our work.

Samples	Conductivity	Li-Li Cyclability	Li-LFP cyclability	Reference
LAGP@PAN/PVCA	2.05 × 10^{-4} S cm^{-1} at 30 °C	2300 h at 0.1 mA cm^{-2}	88 % after 700 cycles at 1C	[1]
LATP-based LPL@GPE	7.98 × 10^{-4} S cm^{-1}	1116 h at 0.2 mA cm^{-2}	97.2% after 240 cycles at 0.5C	[2]

LLZTO and P(VDF-HFP) based CPE-3	1.70×10^{-3} S cm^{-1} at 30 °C	1000 h at 0.1 mA cm^{-2}	88.67% after 500 cycles at 1C	[3]
TAEI, FEC, TTFEP-based GPE	1.1×10^{-3} S cm^{-1} at 30 °C	1200 h at 0.5 mA cm^{-2}	96.6% after 800 cycles at 1C	[4]
QSE with LiDFOB	2.66×10^{-4} S cm^{-1}	600 h at 0.3 mA cm^{-2}	98.54% after 400 cycles at 1C	[5]
$Al(OTf)_3$-DOL-based	1.5×10^{-4} S cm^{-1}	650 h at 1 mA cm^{-2}	94.5% after 300 cycles at 1C	[6]
PDOL-FEC-GTE composite electrolyte	2.1×10^{-4} S cm^{-1}	790 h at 1 mA cm^{-2}	84.1% after 200 cycles at 1C	[7]
DOL-based composite electrolyte	**3.6×10^{-4} S cm^{-1}**	**3000 h at 0.2 mA cm^{-2} &**	**111 mAh g^{-1} at the**	**This work**

		100 h at 1 mA cm^{-2}	**262nd cycle & 107 mAh g^{-1} at the 500th cycle**	

References

[1] H. Feng, Z. Li, S. Gao, Y. Zhang, R. Guo, P.F. Cao, H. Yang, Interface compatible organic-inorganic solid electrolyte with intimate electrode/electrolyte interfacial contact for dendrite-free Li metal batteries, J. Colloid Interface Sci., 702 (2026).

[2] K. Cui, Y. Du, S. Zhang, L. Wang, Y. Fan, A symmetric composite electrolyte for enhancing performance and practicality of lithium metal batteries, Mater. Lett., 403 (2026).

[3] J. Liao, W. Yuan, S. Huang, D. Song, Q. Su, C. Li, J. He, In situ polymerization on a novel support skeleton to form a composite gel polymer electrolyte for high temperature lithium metal batteries, Mater. Res. Bull., 192 (2025).

[4] C. Xu, Z. Fan, J. Huang, L. Xu, B. Ding, X. Zhang, Long-cycling lithium metal batteries enabled by fluorinated and phosphate additive-engineered gel electrolytes, Chem. Eng. J., 523 (2025).

[5] Y. Liu, F. Xu, C. Wang, X. Cao, J. Cheng, Z. Zeng, H. Yao, Y. Xu, LiDFOB-Regulated interfacial chemistry enables high-coulombic-efficiency elastomeric electrolytes for lithium metal batteries, Appl. Surf. Sci., 708 (2025).

[6] H. Huang, C. Wei, Q. Zhao, A. Zhou, J. Li, An initiator loaded separator triggering in situ polymerization of a poly(1,3-dioxolane) quasi-solid electrolyte for lithium metal batteries, Phys. Chem. Chem. Phys., 26 (2024) 20273-20279.

[7] H. Huang, L. Yi, X. Chen, C. Wei, A. Zhou, Y. Wang, J. Li, A glycerol triglycidyl ether cross-linker assisting an in situ thermally polymerized gel polymer electrolyte for advanced lithium metal batteries, New J. Chem., 48 (2024) 13631-13638.